AGU PUBLICATIONS

JGR

Journal of Geophysical Research: Solid Earth

RESEARCH ARTICLE

10.1002/2017JB014525

Key Points:

- Detailed slip model of Kumamoto earthquake sequence resolved
- Innovative model parameterization adopted in inversion
- Effects of “material” and “stress” barriers classified and discussed

Supporting Information:

- Supporting Information S1
- Table S1
- Table S2
- Table S3

Correspondence to:
H. Yue,
yue.han@pku.edu.cn

Citation:
Yue, H., Ross, Z. E., Liang, C., Michel, S., Fattahi, H., Fielding, E., … Jia, B. (2017). The 2016 Kumamoto $M_w = 7.0$ earthquake: A significant event in a fault–volcano system. *Journal of Geophysical Research: Solid Earth*, *122*, 9166–9183. https://doi.org/10.1002/2017JB014525

Received 5 JUN 2017
Accepted 18 OCT 2017
Accepted article online 20 OCT 2017
Published online 27 NOV 2017

The 2016 Kumamoto $M_w = 7.0$ Earthquake: A Significant Event in a Fault–Volcano System

Han Yue[1], Zachary E. Ross[2], Cunren Liang[3], Sylvain Michel[2,4], Heresh Fattahi[2], Eric Fielding[3], Angelyn Moore[3], Zhen Liu[3], and Bo Jia[1]

[1]School of Earth and Space Sciences, Peking University, Beijing, China, [2]Seismological Laboratory, California Institute of Technology, Pasadena, CA, USA, [3]Jet Propulsion Laboratory, California Institute of Technology, Pasadena, CA, USA, [4]Department of Earth Sciences, University of Cambridge, Cambridge, UK

Abstract The 2016 Kumamoto earthquake sequence occurred on the Futagawa–Hinagu fault zone near the Aso volcano on Kyushu island. The sequence was initiated with two major ($M_w \geq 6.0$) foreshocks, and the mainshock ($M_w = 7.0$) occurred 25 h after the second major foreshock. We combine GPS, strong motion, synthetic aperture radar images, and surface offset data in a joint inversion to resolve the kinematic rupture process of the mainshock and coseismic displacement of the foreshocks. The joint inversion results reveal a unilateral rupture process for the mainshock involving sequential rupture of four major asperities. The slip area of the foreshocks and mainshock and the aftershock loci form a detailed complementary pattern. The mainshock rupture terminates near the rim of the caldera, leaving a ~10 km long gap of aftershocks. This area is characterized by high temperature and low shear wave velocity, density, and resistivity, which may be related to the partially melted geothermal condition. Ductile material property near the volcano may act as a “material barrier” to the dynamic rupture. Topographic weight of the caldera increases compressional normal stress on the fault plane, which may behave as a “stress barrier.” Long-term seismic hazard and deformation behaviors related to these two types of barriers are discussed in terms of the associated frictional mechanism. Significant postseismic creeps observed near the volcano area indicates a velocity strengthening frictional behavior near the rupture termination, which confirms that the “material barrier” mechanism is likely the dominant rupture termination mechanism.

1. Introduction

In April 2016, a series of earthquakes occurred on the Futagawa–Hinagu fault zone in Kyushu island. The mainshock was a strike slip event (15 April 2016, 16:25:06, USGS PDE catalog, $M_w = 7.0$ GCMT) and was preceded by many foreshocks including two $M_w \geq 6.0$ events. These major foreshocks (14 April 2016, 12:26:40, $M_w = 6.2$, and 14 April 2016, 15:04:60, $M_w = 6.0$ GCMT) occurred on a subvertical fault plane dipping slightly to the east. The mainshock occurred 25 h after the second major foreshock on a different fault plane dipping (77° GCMT) to the northwest (Figure 1). The focal mechanism of the mainshock is dominated by strike-slip motion, with an approximately 30% of normal slip component (strike/dip/rake: 222°/77°/−161°, GCMT; Ekström et al., 2012). The mainshock rupture initiated near the foreshocks and propagated unilaterally to the NE direction, terminating close to the Aso caldera. The vertical coseismic displacement field displays a four-lobed pattern with prominent subsidence on the NW side (Figure 1). This is consistent with the combination of strike slip and normal faulting revealed in the point source solution. The center of the four lobes is near the rim of the caldera, indicating a strong slip gradient at the rupture terminus (Figure 1).

Kato et al. (2016) use the Hi-net data to relocate aftershocks and demonstrate that the foreshocks and aftershocks that occurred on different fault planes. Downdip migration of foreshock activities is reported, which may be related to the initiation of the mainshock. The kinematic rupture process of the Kumamoto mainshock was also investigated using teleseismic, regional strong-motion, and GPS data sets (Hao et al., 2017; Kubo et al., 2016; Lin et al., 2016; Yagi et al., 2016), which all indicate a unilateral rupture process. Lin et al. (2016) suggest that the termination of the coseismic rupture near the Aso volcano is due to the presence of a localized magma chamber. The structure of the Aso volcano has been investigated by magnetotelluric (Hata et al., 2016) and gravity surveys (Miyakawa et al., 2016). These studies show high-conductivity and low-gravity anomalies beneath the caldera of the Aso volcano, which may be related to the existence of a magma chamber. This is also consistent with the low-velocity and high-attenuation velocity structure

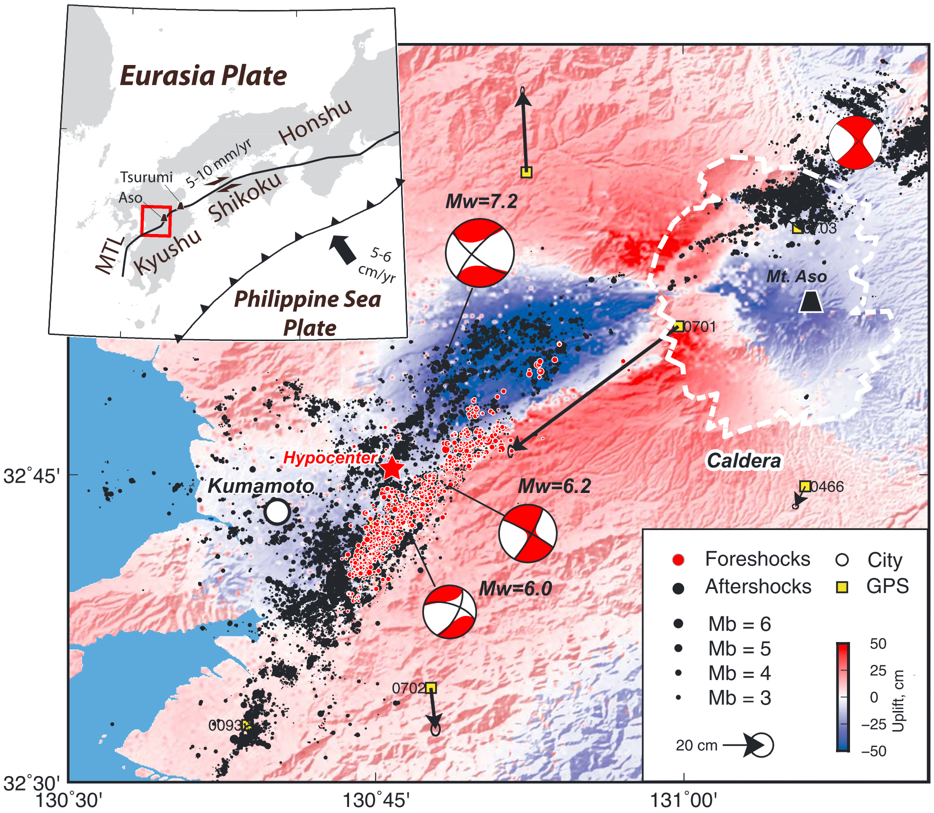

Figure 1. GCMT solutions of significant foreshocks, aftershocks, and mainshock are plotted with red-filled focal mechanisms. Relocated foreshocks and aftershocks are plotted with red- and black-filled circles, respectively. The cone of mountain Aso is marked with a black-filled trapezoid with the caldera rim marked with dashed white curves. GPS stations are marked with yellow-filled squares with the recorded coseismic horizontal displacements plotted with black arrows. Coseismic uplift field of the Kumamoto earthquake sequence calculation from 3-D displacement field reconstruction using SAR data is plotted with a blue-red color scale as the background. The Kumamoto city is plotted with a white filled circle. The regional coast map is plotted on the top left with the plate boundary between the Eurasia and Philippine plate marked with a barbed line. Land area is filled with gray. The plotting area is marked with a red bounded rectangle.

resolved by seismic surveys (Okubo et al., 1989; Sudo & Kong, 2001; Tsutsui & Sudo, 2004; Unglert et al., 2011; Yasuaki Sudo, 1991).

Faults and volcanos are two geologic settings that cause devastating natural disasters. The interaction between faults and volcanos is of interest to understand the mechanisms of earthquake ruptures and volcanic eruptions (Azzaro, 1999; Nishigami, 1997), for example, the behavior of ruptures in geothermal environments (Duquesnoy et al., 1994) and whether volcanic eruptions are triggered by earthquakes (Linde & Sacks, 1998; Moran et al., 2002). Significant earthquakes hosted by tectonic faults near volcanic areas provide an opportunity to understand related scientific problems (Ando & Okuyama, 2010; Moran et al., 2002). The Median Tectonic Line (MTL) is the longest onshore fault system of Japan (Figure 1), which cuts through the islands of Honshu, Shikoku, and Kyushu (Wibberley & Shimamoto, 2003). It has a right lateral sense of motion and slips at a rate of 5–10 mm/yr (Okada, 1973), which is consistent with the oblique convergence direction at the Nankai trough. On Kyushu island, the MTL is shearing at around 7 mm/yr (Nishimura & Hashimoto, 2006; Wallace et al., 2009) and actively producing seismicity (Matsumoto et al., 2015), yet no significant ($M_w > 7.0$) events on the MTL were recorded historically before the 2016 Kumamoto event. It is not certain that the Futagawa–Hinagu fault is the key fault producing the observed geological contrast across the MTL in history, yet the 2016 Kumamoto event is a significant event that contributes to the cumulated offset along the MTL and releases tectonic stresses. We infer that stresses on the MTL is currently accumulated and released on the Futagawa–Hinagu fault zone, and the 2016 Kumamoto earthquake is a tectonic event. The Aso and the

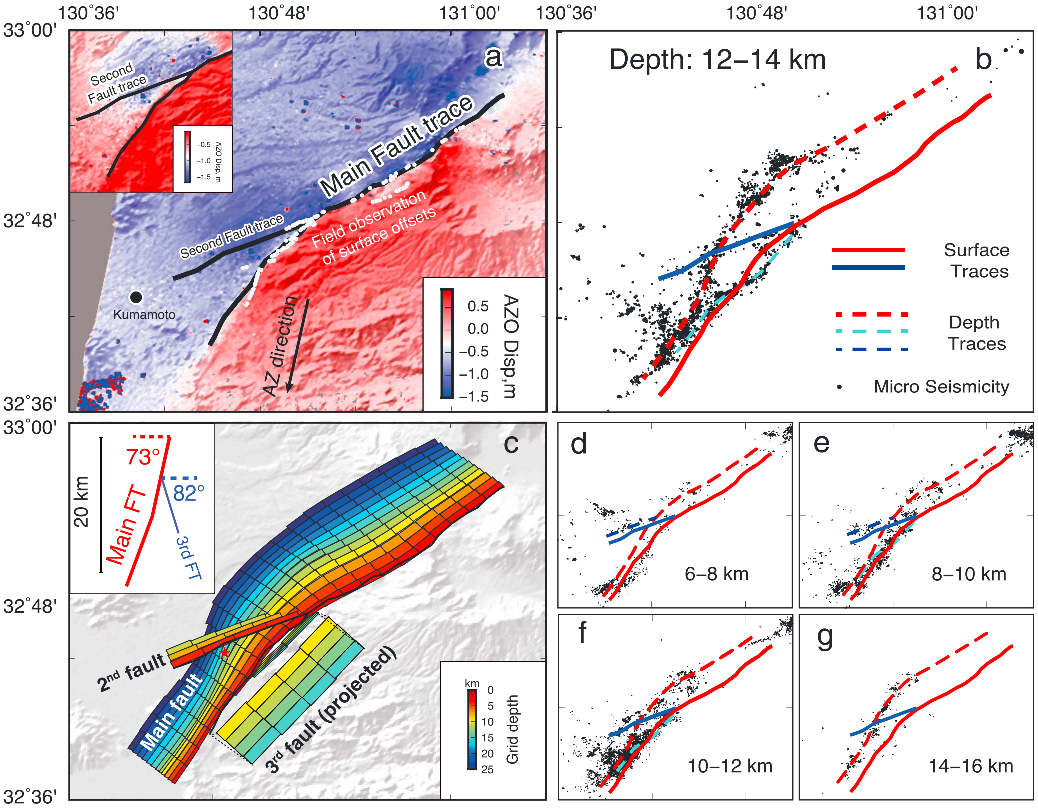

Figure 2. (a) Coseismic displacement projected to the SAR azimuth direction (azimuth offset, AZO) is plotted with a blue to red color scale. The azimuth direction is indicated with a black arrow. Two fault traces are identified from the offset in AZO images and plotted with black curves. Surface offsets obtained by a field observation (Shirahama et al., 2016) are marked with white filled circles. AZO displacement near the second fault trace is plotted with a different color scale in the inserted map (top-left) to emphasize the location of the second fault trace. (b) Fault traces related to three fault segments are plotted in red, blue, and cyan, respectively. The fault traces at the surface and at 13 km depth are plotted with solid and dashed curves, respectively. Aftershocks relocated between 12 and 14 km depth are plotted with black dots, which is used to identify fault traces at depths. (c) Subfaults of the fault model are plotted with color-coded rectangles with the hypocentral depth indicated by the filling color. The third fault plane is subvertical (85° dipping to the southeast), yet projected as 45° dipping for visualization. A side view of the first and third fault planes is plotted in red and blue in an insert map on the top left. (d–g) The same as Figure 2b yet plotted for different depth cuts.

Tsurumi volcanoes are coincident with the MTL (Figure 1), which provides a tectonic site to study how active faulting interacts with active volcanos.

The Japanese islands are instrumented with dense seismic and geodetic networks, that is, Hi-net, K-net and KiK-net, and Geo-net, which recorded the dynamic and coseismic ground motion during the Kumamoto earthquake sequence. The dense near-field observations allow for determination of a high-resolution kinematic rupture process. This study focuses on using regional seismic and geodetic data sets in a joint inversion to determine the rupture process of the Kumamoto earthquake sequence in high resolution. We further discuss the triggering relationship and rupture mechanisms of the Kumamoto earthquake sequence.

2. Data and Methods

2.1. Fault Model Parameterization

Previous studies indicate that curved and segmented faults are involved in the rupture process of the Kumamoto earthquake sequence (Hao et al., 2017); thus, the fault plane needs to be parameterized precisely before the inversion is performed. Two techniques are adopted to parameterize the curved and segmented fault planes. We identify the surface fault trace from ground displacement field images and identify fault traces at depth from the aftershock hypocenters. We apply the pixel tracking technique (Liang & Fielding,

2016) to high-resolution (Ultrafine mode) synthetic aperture radar (SAR) images recorded by the Japanese Aerospace Exploration Agency (JAXA) Advanced Land Observing Satellite 2 (ALOS-2) on a descending orbit (path D23), which reflects the coseismic horizontal ground displacement field projected to the azimuth or along-track direction (azimuth-offset AZO; Figure 2a). Opposite displacement directions are imaged on two sides of the fault, and the fault trace can be clearly identified from the discontinuities in displacement fields (Figure 2a). A secondary fault trace is also identified from the AZO image on the northwest side of the main fault trace, which presents ~20 cm offset in the azimuth direction (Figure 2a). Surface ruptures were consistently observed by field geologists throughout the fault trace, and the peak displacements are identified near the caldera (Himematsu & Furuya, 2016; Lin et al., 2016; Shirahama et al., 2016). The identified surface trace is consistent with that obtained by field observations (Figure 2a).

Previous studies indicate that different fault planes are involved in the rupture of the foreshocks and mainshock (Asano & Iwata, 2016; Kato et al., 2016) and the foreshocks appear to have occurred on a hidden or blind fault plane. To better constrain the complex fault geometry at depth, we applied a template-matching algorithm to significantly expand the catalog of events (Ross et al., 2016; Shelly et al., 2016). Templates were constructed using automated *P* and *S* wave phase picks (Ross et al., 2016), with *P* wave templates taken from vertical components and *S* wave templates taken from both horizontal components. The template-matching procedure resulted in 63,336 events detected during the period with at least four differential times. These differential times were then used as an input to the GrowClust relocation algorithm (Trugman & Shearer, 2017), requiring at least eight differential times with a minimum correlation coefficient of 0.6. This entire process resulted in 36,543 precisely located earthquakes, including 840 foreshocks and 35,703 aftershocks, which are plotted at different depths in Figures 2b, 2e, and 2f. Relocated catalog are provided in the supporting information.

Lineation of microseismic activities are most significant at 12–14 km depths, and two lineated fault traces can be detected from the location of the microseismicities, which appear to be associated with the NW dipping main fault plane and the subvertical fault plane that host the foreshocks (Figure 2b). Fault traces at other depths (Figures 2d–2g) also present some level of lineation, yet not as clear as the 12–14 km depths. Off-fault cracks may be activated at shallow depths that mix with on-fault seismicities. Therefore, the fault geometry is mainly a parameterized reference to the surface trace and seismicity at the 12–14 km depth (Figure 2). Three distinct fault planes can be identified from the aftershock locations, and fault traces are sketched from the aftershock distribution at each depth (Figure 2). There is a seismic gap around 32.9°N located at the northern end of the coseismic rupture; therefore, fault traces for the northern half of the main fault plane are not identified from the aftershock locations. For simplicity, we extended the straight fault trace from the center to the northeastern end to introduce a uniform dip angle. Fault planes are parameterized by connecting the fault traces at different depths and discretized into subfaults (Figure 2c). Three fault planes are used in the inversion, with the main fault plane being approximately 40 km long with a curved geometry. The averaged dip angles of the southern and northern parts are 73° and 65°, respectively. The second fault trace are identified from the secondary surface rupture and the associated shallow seismicity ($<$10 km), which is a ~10 km long fault plane dipping to the northwest that connects with the main fault plane at its northeastern end. The major foreshocks are hosted by the third fault plane, which is parameterized from the foreshock distribution and the GCMT focal mechanism of the major foreshocks. The third fault plane is subparallel to the main fault plane but dips slightly (85°) to the east. It is unclear if the aftershocks occurred on the main or third fault plane above 8 km. If two fault planes coexist above 8 km depth in a subparallel sense, they are too close to be separated by the inversion. Therefore, we parameterize the third fault plane as a hidden fault located beneath 10 km depth, which is consistent with the fault trace identified by Kato et al. (2016). The major foreshocks appear to have occurred on both the main and third fault planes, which will be discussed in the following sessions. Fault crossing profiles are plotted in Figure S1, which reveals the cross section of the seismicity and fault model at different segments.

2.2. Data

We used four types of data in a joint inversion to resolve both the spatial and temporal information of the kinematic rupture process of the Kumamoto earthquake sequence. The seismic data include three-component ground acceleration waveforms of the mainshock recorded by nine K-net and KiK-net strong motion stations (Figure 3 and S2). Although stations at further distance are available, the azimuth

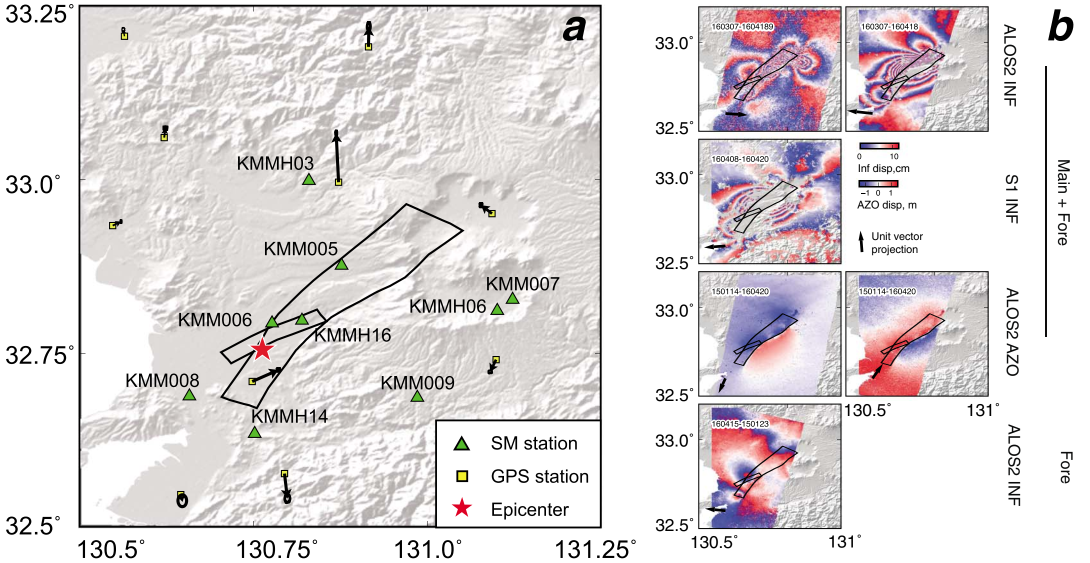

Figure 3. (a) The mainshock epicenter location is indicated with a red filled star. Boundaries of the first and second fault planes are plotted with black curves. GPS stations are plotted with yellow filled squares. Strong motion stations are plotted with green filled rectangles. (b) SAR images are plotted in each panel. The interferograms recorded by ALOS2 and Sentinal1 (S1) satellites are plotted in the first two rows. Azimuth offsets derived from two ALOS2 images are plotted in a blue to red color scale. Interferogram of the foreshocks recorded by the left-looking ALOS2 satellite are plotted in the fourth row.

coverage of the adopted stations is good enough to capture the rupture directivity. Green's function calculation for more distant stations requires more accurate reference model, which brings more uncertainty of the current reference model. Therefore, we only adopted relatively close stations. Original ground acceleration data are integrated to calculate velocity waveforms, which are directly used in the inversion. A frequency–wavenumber integration method (Zhu & Rivera, 2002) is used to calculate velocity Green's functions for each strong motion station reference to the respective local velocity model at each station. The generation of local velocity layer is discussed in the next session.

We use Geo-net GPS displacement data from 10 three-component stations for both the foreshocks and the mainshock (Figure 3). Original GPS data sampled at 30 s are processed to obtain solutions at a 20 min interval using kinematic precise point positioning with GIPSY-OASIS (Zumberge et al., 1997) and single station ambiguity resolution (Bertiger et al., 2010). Both static and kinematic processing fixed the GPS satellite orbits and clocks to the JPL FLINN final orbit products (Desai et al., 2009). The IGS antenna phase center variations were applied to reduce errors due to antenna-specific azimuthal and elevation-dependent changes in antenna phase center (Schmid et al., 2007). We extract coseismic displacements that occurred during the foreshocks and mainshock from the continuous GPS time series. The coseismic displacements of the mainshock are determined by the offset that occurred before and after the mainshock. The coseismic displacements of the foreshocks are determined by the offset that occurred before the first major foreshock and after the second major foreshock. To estimate GPS offsets, GPS time series are averaged over 3 h time windows centered at the target time point to retrieve GPS position more accurately. Displacements are thus estimated from position differences. GPS station 0701 (Figure 1) is the closest GPS station to the fault trace, which recorded coseismic displacement of ~1 m. This station locates within kilometers from the fault trace and thus is only sensitive to the local slip amount. On the other hand, stations too close to the fault trace suffer from the uncertainty of model parameterization and nonelastic response of the near fault medium, which may not be properly modeled by Green's functions. For the above reasoning, we did not include station 0701 in the inversion.

We consider six SAR-based measurements of the coseismic displacement field produced by interferometric SAR (InSAR) and SAR pixel tracking techniques (Figure 2d) using the InSAR Scientific Computing Environment (Rosen et al., 2012). We obtained focused radar images from the JAXA Advanced Land

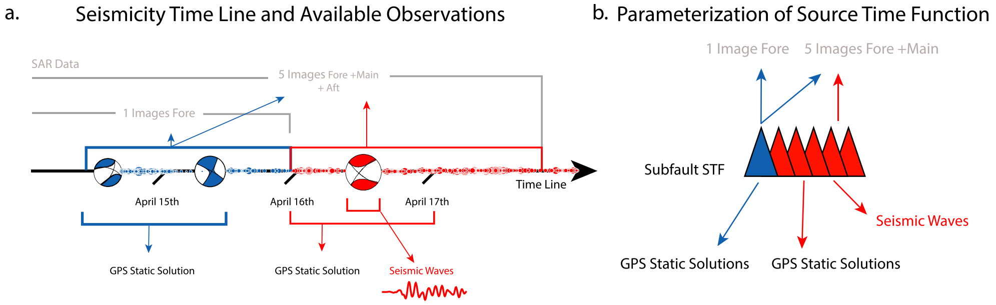

Figure 4. (a) A cartoon shows the data used in joint inversion and the contribution of the foreshocks and mainshocks to each data set. Two major foreshocks and the mainshock are plotted in blue and red filled focal mechanisms projected on the time axis. Time span of six SAR images are marked on the top of the time arrow with the contribution from each event indicated by blue and red arrows, respectively. The coseismic displacements of both the main and foreshocks recorded by GPS stations are used in the joint inversion. The dynamic waves of the mainshock recorded by strong motion stations are used in inversion. (b) Parameterization of the source time function of each subfault on the main fault plane is indicated by blue and red filled triangles, respectively. The first triangle presents the coseismic slip during the foreshock period, and the red triangles present the dynamic rupture process during the mainshock period. The contribution to each data set from each parameter is indicated with blue and red arrows.

Observing Satellite 2 (ALOS-2) and the Copernicus Sentinel-1A satellite processed by the European Space Agency. Five SAR image pairs recorded the coseismic deformations of both the mainshocks and foreshocks, yet one SAR image pair with an acquisition between the mainshock and second major foreshock recorded the deformation that happened during the foreshock period (Table S1). Information of all SAR data is summarized in Table S1, and SAR data processing (Liang & Fielding, 2016; Rosen et al., 2012) and sampling details are described in the supporting information.

We calculated the ground horizontal displacement field from subpixel correlation of pre-earthquake and postearthquake satellite optical images using the COSI-Corr software (Coregistration of Optical Sensed Images and Correlation; Leprince et al., 2007; Ayoub et al., 2009). Two Landsat-8 panchromatic images (15 m resolution) from 21 May 2015 to 23 May 2016 were used, taking into account a time period that includes the foreshocks, the mainshock, and the early postseismic deformation of the Kumamoto earthquake. Horizontal offsets across the surface fault trace are obtained by line fitting the near-field displacement on each side of the fault. The fault normal and parallel components of the displacement at the fault trace are then used in the inversion to constrain the right lateral and normal slip components of the coseismic slip of the foreshocks and mainshock.

For both the SAR and optic images, the postseismic deformation over a short period ($<$1 week) are included in the displacement field, which can potentially cause overestimated coseismic slips. Displacement time series recorded by GPS stations close to the fault show that the postseismic displacement occurred within 1 week after the mainshock is less than 10% of the coseismic displacement. Considering the observational and modeling errors of the inversion process, the postseismic introduced errors are neglected. More details of the data information and processing techniques are provided in the supporting information.

2.3. Multi-Time-Window Parameterization

We adopted the multi-time-window (MTW) inversion method to parameterize the kinematic rupture process (Hartzell & Heaton, 1983). In traditional MTW inversion techniques, each of the multiple triangles is shifted by the half-duration to create the source time function (STF) of each subfault. For the case of the Kumamoto earthquake, five SAR images recorded the ground deformation of both the foreshocks and the mainshock; therefore, traditional inversion algorithms (e.g., Yue et al., 2014; Yue & Lay, 2013) cannot discriminate the slip between the two periods. To discriminate foreshock and mainshock slips, we use one triangle to represent the moment released by foreshocks and the remaining triangles to represent the kinematic rupture process during the mainshock. The contributions to each data set are demonstrated in Figure 4b, which is used to guide the construction of Green's function matrix (Gmat). Gmat can be viewed as a projection from model space to the data space. The element of Gmat, at the *i*th column and *j*th row, presents the contribution from the *i*th inversion parameter to the *j*th data point. In our parameterization, the particular Gmat element is set to 0 when there is no contribution between the related inversion parameter and data point. This parameterization method enables the inversion to discriminate the slip that occurred during the foreshocks and mainshock and invert for both slips simultaneously. In this paper, we focus on the kinematic rupture process of the mainshock; thus, only the static slip during the foreshock period is inverted.

Green's functions are calculated for two slip vectors at a rake angle of 200 ±45°. A nonnegative linear least squares inversion (Lawson & Hanson, 1995) is performed, which allow both normal and strike-slip components in the inversion results. Four triangles with half-duration of 2 s are used to parameterize the STF of each subfault of the mainshock, which enables a 10 s long subfault source duration. We parameterize the Kumamoto earthquake sequence as three "conceptual subevents," in which the first event represents the kinematic rupture during the mainshock that occurred on the main fault plane; the second event represents the static slip during the foreshock period that occurred on the main and third fault planes; the third event represents the static slips of the mainshock that occurred on the second and third fault planes. Thus, the "coseismic" slip we obtained for the second and third "conceptual" events represents the "accumulated" slip happened during the foreshock period. The status of each subevent and their associated contribution to each data set are summarized in Table S2. Green's functions for strong motion recordings are generated with a frequency–wavenumber integration code (Zhu & Rivera, 2002) for each strong motion station with respect to the local 1-D velocity structure. Two velocity models are used to construct local 1-D velocity structure: deeper velocity structure ($>$5 km) is interpolated from three-dimensional tomography of entire Japan (Matsumoto et al., 2015); shallow velocity structure is interpolated from that provided by J-SHIS of the NIED (Fujiwara et al., 2009, 2012). The reconstructed velocity model accounts for the amplification effect introduced by a shallow sediment layer at each station. The same velocity models and similar construction methods are adopted by Asano and Iwata (2016) to compute GFs for strong motion data. Green's functions for static ground displacement are based on the Wang et al. (2003) reference to a uniform 1-D velocity structure of the source area.

There are several strong motion stations located above the fault plane, which provide tight constraints to the rupture kinematics. Inversions with different rupture velocities are performed to search for the true rupture velocity (Yue, Lay, Freymueller, et al., 2013; Yue, Lay, Schwartz, et al., 2013). A constant rupture velocity of 3.0 km/s is required to avoid truncation of moment rates at the beginning of each subfault STF. Therefore, the rupture velocity is estimated to be 3.0 km/s. There is no significant evidence for a supershear rupture velocity (Yue, Lay, Freymueller, et al., 2013). We adopt an empirical weighting technique (Yue et al., 2017) to determine the relative weighting between each data set. Laplacian smoothing is applied to the model parameters, and the smoothing amplitude is selected to ensure that the deduced Coulomb stress is consistent with the aftershock distribution.

3. Results and Discussion

3.1. Rupture Model of the Mainshock

Our preferred slip model is plotted in Figure 5, and the fits to all data sets are provided in Figures S2–S5. Reasonable fits are achieved for all data sets, with variance reduction of 94%, 86%, 91%, and 91% achieved for the static GPS, strong motion, SAR images, and pixel offset data, respectively. For the SAR images, the average variance reduction for the interferogram and azimuth offset is ~ 90% and ~80% (Figure S3), respectively. Histograms of the residual distributions are plotted for each image in Figure S3. Fits to the fault-parallel offsets are better than that of the fault-normal offsets. Because we parameterized the coseismic slip with oblique slips instead of slip partitioning that occurred during the dynamic rupture processes (dynamic slip partitioning; Himematsu & Furuya, 2016), which is observed in the field measurements, fits to the detailed surface offset pattern is not realized. Our model exhibits an increased amount of normal-faulting slip near the northeastern end of the surface trace, which is consistent with the observed surface offsets (Figures S5 and S6). Details of fault parameterization philosophy and the associated trade-offs with offset fits are discussed in the following sections.

Figure 5 presents a clear unilateral rupture propagating toward the northeast. We can identify at least four concentrated slip areas (asperities) that ruptured sequentially from the hypocenter to the northeastern direction. The first asperity locates near the hypocenter with peak slip of 4 m. The second asperity locates downdip from the hypocenter at ~ 20 km depth with peak slip of 3 m. The third asperity locates ~10 km from the

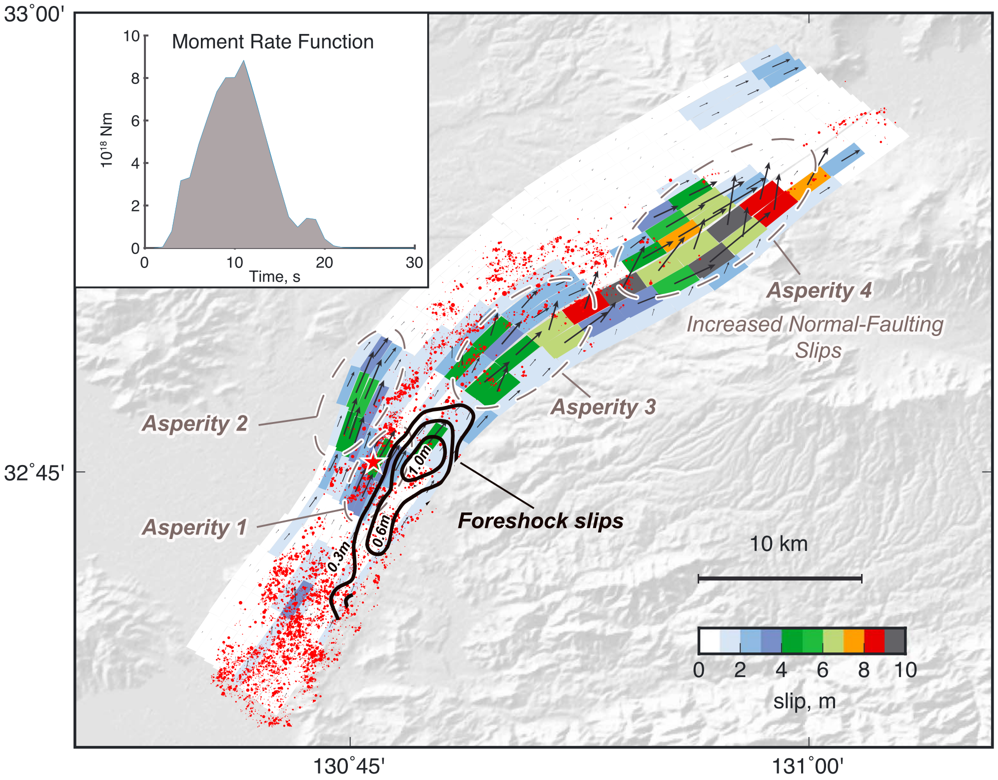

Figure 5. Coseismic slip of the mainshock is plotted for each subfault. Four asperities ruptured sequentially are marked by black dashed ellipsoids. Slip that happened in the foreshock period is plotted with black counters. The mainshock hypocenter is marked with a red-filled star. Aftershocks located within 2 km from the fault plane are plotted with red dots. The total moment rate function of the mainshock is plotted as gray filled polygons in the top-left inserted figure.

hypocenter at ~10 km depth with peak slip of ~ 4 m. The fourth asperity is the strongest asperity in the entire rupture process, and the peak slip of 10 m locates 20 km from the hypocenter at ~ 5 km depth. The fourth asperity is located right under the caldera, with slip rapidly decreased beyond it, introducing a significant along-strike slip gradient at the northeastern end of the rupture area. This is consistent with the prominent surface deformation field observed there (Figure 1). Slip distribution viewed in the fault normal direction is plotted in the supporting information (Figure S7). Various peak slip amounts are reported in published slip models, and the peak slip value of this study is at the higher end of those values. It is noted that the peak slip in the finite fault model is not a reliably resolved value, depending on the adopted data set, model regularization, and parameterization. Kubo et al. (2016) inverted strong motion recordings to determine the kinematic rupture process and found one dominant asperity at the western side of the caldera with peak slip of 3.8 m. The concentrated slip resolved by Kubo et al. (2016) overlaps with the dense aftershock distribution, which locate between the third and fourth asperities in this study. Lin et al. (2016) used strong motion data for source inversion and found a slip pattern similar to ours with maximum slip of ~6 m. Yagi et al. (2016) performed teleseismic body wave inversion and found a smoothed rupture pattern with maximum slip of 5.7 m. As demonstrated by previous studies, geodetic observations place strong constraints on the slip spatial distribution, and joint inversion achieves better resolution to the slip distribution and slip amounts (e.g., Yue, 2014; Yue et al., 2014). Therefore, our slip model has higher resolution than the slip models determined with only seismic data. The area between the third and fourth asperities coincides with the aftershock loci; this complementary pattern demonstrates an improved resolution from SAR images (Yue et al., 2014). Since the resolution of inversion using data collected on the ground surface decreases with depth, the second asperity is not as well resolved as the other asperities. However, since other models inverted from different data sets (e.g., Hao et al., 2017; Lin et al., 2016) show an asperity at a location close to the second asperity, it appears to be located well. Interferogram and azimuth-offset data (collected by the ALOS-2 satellite) are used by Himematsu and Furuya (2016) to invert

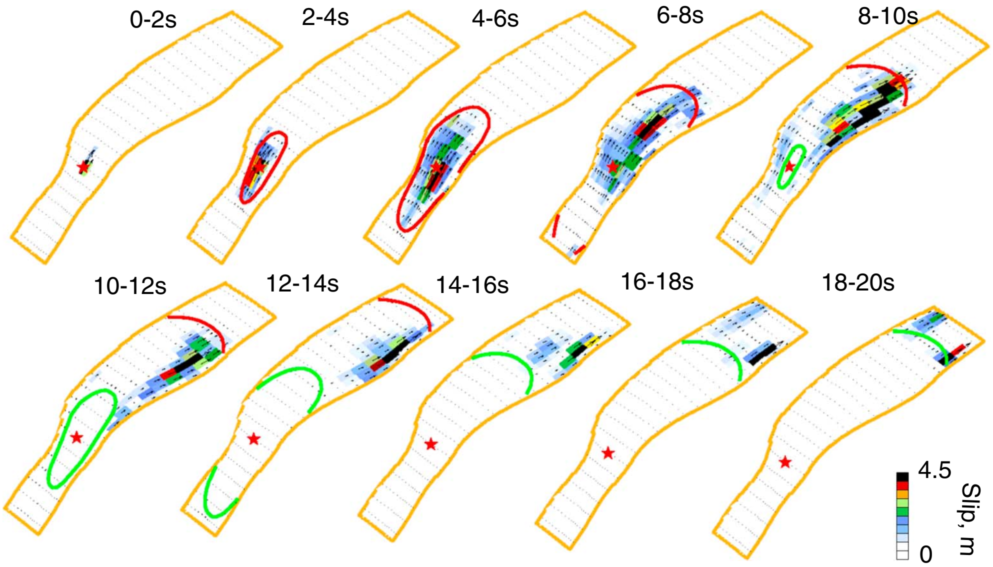

Figure 6. Snapshots of the kinematic rupture process during the mainshock for the preferred slip model are plotted with 2 s interval. Slip amount happened in each time interval is plotted with a white to black color scale. The kinematic expanding of rupture front is indicated by the red (rupture front) and green (healing front) curves.

for the coseismic slip distribution. Two shallow asperities, similar to that resolved by this study, are resolved in their model, which has a maximum right-lateral slip of >5 m and maximum normal slip of 4.5 m. We note that Himematsu and Furuya (2016) parameterize the fault planes with three segments, in which a fault plane subparallel to the main fault plane with 65° dipping angle is parameterized to host the normal slip component. Field and geodetic observations demonstrate that ~2 m of strike-slip and normal faulting displacements are partitioned by two parallel faults, respectively (Kumahara et al., 2016; Lin et al., 2016; Toda et al., 2016). The subsurface geometry of the normal fault is not evident from seismic observations. The dip angle used by Himematsu and Furuya (2016) is similar to the dip angle of the main fault plane in our model, which indicates that the two surface ruptures may merge at depth. Since the resolution of the fault geometry decreases with depth, it is hard to constrain the slip partitioning on adjacent faults. In this study, we simplified the fault model with one curved fault plane, which allows both right-lateral and normal-faulting slips on the main fault plane. Surface displacement fields, within 1 km from the surface fault trace, are excluded from the SAR images for the inversion. We used the fault-parallel and fault-normal offsets, obtained from the satellite optical images, to constrain the slips in the top row; thus, the reported slip partitioning is represented by oblique slips in our model. As noted by Himematsu and Furuya (2016), slip partitioning on separated faults cannot explain the observed ~50 cm of subsidence at the western part of Mt. Aso. This indicates oblique slips probably occurred at deeper depths as shown in our model. Our model has a simplified slip pattern that can explain ground deformation in the far field (>1 km from the surface trace) but is still compatible with the possibility of dynamic slip partitioning. Parameters of the kinematic rupture model of the mainshock and coseismic slip model of the foreshock are provided in the supporting information.

Rupture kinematics are shown as snapshots in Figure 6. The local rupture velocity may be higher than the prescribed rupture velocity (3.0 km/s). For example, during 4–8 s and 10–14 s, the distance between the peak slip location and the prescribed rupture front is reduced, which indicates that the rupture may be propagating faster than the prescribed rupture front. The third and fourth asperities rupture at these two periods. Large slips are associated with higher stress concentrations near the crack tip, which can introduce localized high rupture velocity in nonsteady-state rupture propagation (Beroza & Mikumo, 1996). It is difficult to soundly constrain local rupture velocities without dense near-fault observations; therefore, there is a possibility that the two asperities ruptured at higher rupture velocities. The averaged rupture velocity is soundly constrained by the near-field seismic observations, and we find no evidence that supports a supershear rupture velocity, which has been reported for several large strike-slip events.

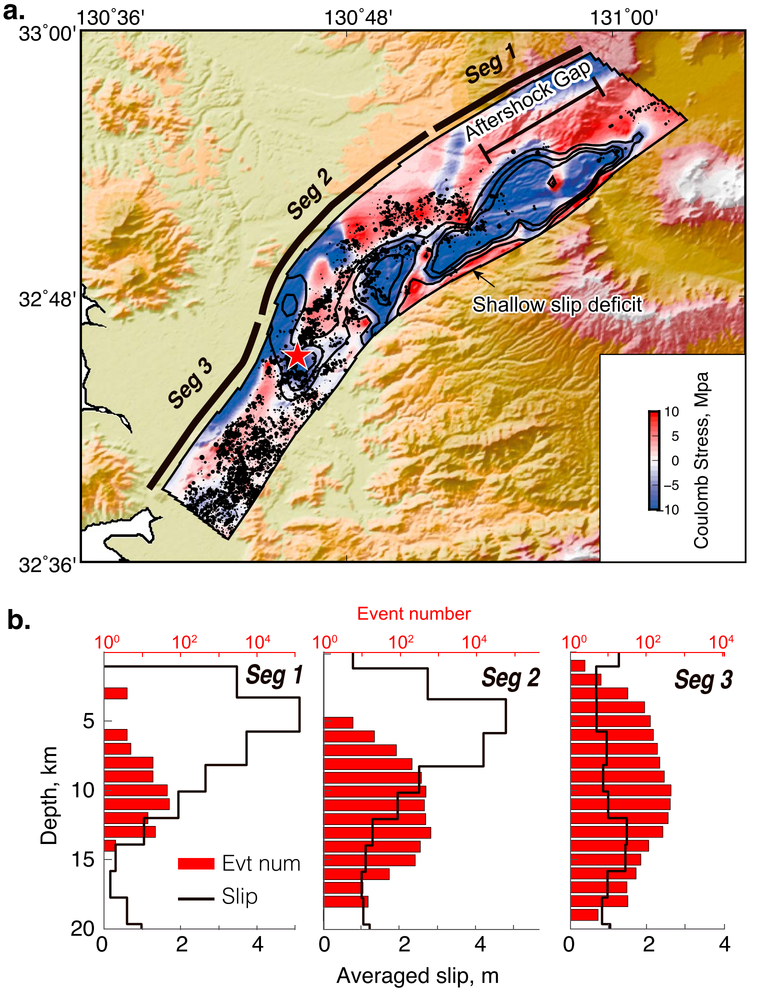

Figure 7. (a) Coulomb stress change caused by the mainshock coseismic slip is imaged with a blue to red color scale. The epicenter location is marked with a red-filled star. Coseismic slip pattern is plotted with black contours. Aftershocks located within 2 km from the fault plane are plotted as black dots. The segment of an aftershock gap where Coulomb stress is increased significantly is indicated by a black line. Lateral extent of three segments are marked by thick black curves and used to calculate slip/seismicity histograms in Figure 7b. (b) Depth distribution of the catalog event number occurred within each segment are plotted with red filled histograms as a log-scale in each panel, respectively. Mainshock coseismic slips occurred in each segment are averaged at each depth and plotted with black curves.

3.2. Shallow Slip Deficit

Significant shallow slip deficit (>30%) occurs in the region updip of the three shallow asperities (Figure 5). Shallow slip deficit is defined as (peak slip at depth − shallow slip)/peak slip at depth, which relies on the estimation of slips occurred at both shallow and deep depths. Slips along fault surface in our model is well estimated from SAR AZO and optic offset data, so that fault parallel slip smaller than 3 m is generally resolved along the surface rupture, which is consistent with the surface offsets measured by field observations (Lin et al., 2016). The peak slip at depth is not as well constrained as shallow slips, which strongly relies on the selected inversion parameters. We test inversion with different parameters, and significant shallow slip deficit (30%–50%) is resolved in all results, which by all means is significant (Lapusta et al., 2000). Shallow slip deficits may be caused by velocity-strengthening friction at shallow depths (Marone, 1998; Rice, 1993; Rice et al., 2001), thick sedimentary layers with overpressurized pore fluids (M. Wei et al., 2011), or bulk inelastic yielding of the shallow brittle host rock (Fielding et al., 2009; Kaneko & Fialko, 2011). A combination of different mechanisms may produce large (>30%) shallow slip deficit. If shallow slip deficits were caused by velocity strengthening friction, after slip will happen at shallow depths (Lapusta et al., 2000). This is observed in the postseismic deformation field of the Kumamoto earthquake as discussed in the following sections. Postseismic deformation indicates that velocity strengthening could be an important factor in the observed shallow slip deficit.

3.3. Complementary Pattern Between Mainshocks, Foreshocks, and Aftershocks

The mainshock slip pattern and aftershock hypocenters are found to be complementary for several great earthquakes, for example, the 2010 Maule earthquake (Yue et al., 2014), the 2010 El Mayor-Cucapah earthquake (S. Wei et al., 2011), the 2015 Gorkha earthquake (Avouac et al., 2015; Yue et al., 2017), and the 2015 Illapel earthquake (An et al., 2017; Melgar et al., 2016). Such pattern is precisely resolved for the Kumamoto earthquake. We select aftershocks located within 2 km from the fault plane and overlay them onto the slip model (Figures 5 and 7). A detailed complementary pattern between the mainshock slips and the aftershock loci is revealed by such comparison. Areas with significant coseismic slips are depleted of aftershocks, demonstrating that these asperities are probably locked in the postseismic period. Substantial aftershocks filled the space between asperities, for example, between the third and fourth asperities and near the downdip edge of the coseismic rupture area. These can be triggered by the Coulomb stress increase near the edges of the coseismic slip area (Figure 7). Aftershocks complementary to the coseismic slips can be interpreted with (1) direct triggering from coseismic stress change (Stein et al., 1994) or (2) ruptures that occurred on the brittle creeping fault zone (Perfettini & Avouac, 2004, 2007). For both mechanisms, aftershocks locate in the Coulomb stress increasing area. For the second mechanism, aftershocks are considered as driven by aseismic creeps, which are found to be the dominant moment releasing mechanism in comparison with that released by aftershocks, for example, the Chi-chi earthquake (Perfettini & Avouac, 2004), Landers earthquake (Perfettini & Avouac, 2007), and the Nias earthquake (Hsu et al., 2006). We separate the Kumamoto main fault plane as three segments along the strike direction (Figure 7a) and plot the slip and seismicity depth histograms in Figure 7b. Within the central segment (Seg 2), aftershocks mostly distribute between 10 and 15 km below the depth of peak coseismic slip, which are mainly composed of events located along the bottom of the coseismic slip areas (Figure 7a). These aftershocks may be attributed to the brittle creeping fault zone mechanism, because the depth is consistent with the brittle and ductile transition (Perfettini & Avouac, 2004). Areas at the southwestern end of the main fault plane (segment 3, Figure 7b) present limited postseismic deformation or after slips (Moore et al., 2017), and the microseismicity are widely distributed from 5 km to 18 km, which indicates that the coseismic stress triggering (first mechanism) may be the dominant triggering mechanism. Two areas with substantial Coulomb stress increase present limited aftershocks, that is, the shallow slip deficit area and the downdip edge of the last asperity (Seg 1 in Figure 7b). The seismicity productivity at the NE end is two orders of magnitude less in comparison with that in the central and SW segments, yet this segment produces significant postseismic deformation. The absence of aftershocks and fast postseismic deformation observed in the NE end of coseismic rupture is consistent with the prediction of velocity strengthening frictional property.

The cumulative slip during the foreshock period (foreshock slips) includes the coseismic deformation from the two major foreshocks, as well as the seismic and aseismic after slip following them. The foreshock slips can be independently resolved from the observations that are only contributed by the foreshocks, for example, GPS and SAR observations (interferogram no. 6, Table S1), which is thus used to invert for the foreshock slips (Figure 5). Foreshock slip models resolved by joint and independent inversions are shown in Figures S6 and S7, respectively. The resolved foreshock slip pattern is consistent between these two results with slight differences presented in the centroid slip location and slip distribution. The purpose to include both foreshocks and mainshock in the joint inversion is to prevent misinterpreting foreshock slips as mainshock slips, although slip leaking is inevitable because of errors in observations and in GF computation. In comparison with the large slips of the mainshock, relative slip leaking can be more significant in the foreshock slip model. Therefore, we consider the foreshock slips resolved by the independent inversion to be more accurate than the joint inversion results. The foreshock slips occur updip of the mainshock hypocenter, where a small number of aftershocks occurred (Figure 5). Thus, the foreshock slips are also complementary to the mainshock and aftershocks. The GCMT solution of both $M_w > 6.0$ foreshocks indicates a subvertical fault plane dipping slightly to the east. Asano and Iwata (2016) parameterized the foreshock with single subvertical fault plane and invert for the foreshock slips with strong motion data. They found two concentrated slip areas, one near the foreshock hypocenter and one at shallow depths. However, inversion with multiple point sources resolves the first foreshock ($M_w = 6.2$) as three subevents: the first subevent was east dipping and was followed by two west dipping subevents (Shi et al., 2016). The focal mechanisms of the three point sources are consistent with the two fault planes in our source model; thus, the first major foreshock appears to have ruptured both the east (third) and the west dipping (first) fault planes. We invert the foreshock slips with/without ruptures on the main fault and find that including main fault ruptures increases the variance reduction of the SAR data from 66% to 82%. It demonstrates that slips on the main fault plane are required to fit the geodetic observations (Figure S6). Kato et al. (2016) detected a migration of foreshocks to the deep portion along the main fault plane, which appears to be related to the initiation of the mainshock rupture process. If the first foreshock ruptured on the main fault plane at shallow depths, after slips may have migrated downdip, which increased the shear stress near the mainshock hypocenter and initiated the mainshock rupture. The triggering relationship between the foreshock and mainshock is of interest in order to better understand precursory seismic evidence. The foreshock after slip may be the key factor that initiated the mainshock rupture.

3.4. Termination of the Coseismic Rupture

The mainshock rupture terminated under the caldera, introducing significant Coulomb stress increase to its northeastern end (Figure 7a). A seismic gap is observed at the same location, which is inconsistent with the static stress triggering relationship observed in other parts of the fault. Lin et al. (2016) propose that the coseismic rupturing of the mainshock may have been stopped by a magma chamber. Three-dimensional electrical resistivity structure near the caldera reveals magma pathways beneath the caldera (Hata et al., 2016), which find a secondary low-resistivity zone beneath the western caldera rim. This location appears to be correlated with a partially melted material composition (Lin et al., 2016). Low material density is also resolved at this location, indicating high fluid content (Miyakawa et al., 2016). Receiver function studies reveal a low shear wave velocity layer at 10–24 km depths beneath the Aso caldera (Abe et al., 2010). We interpolate

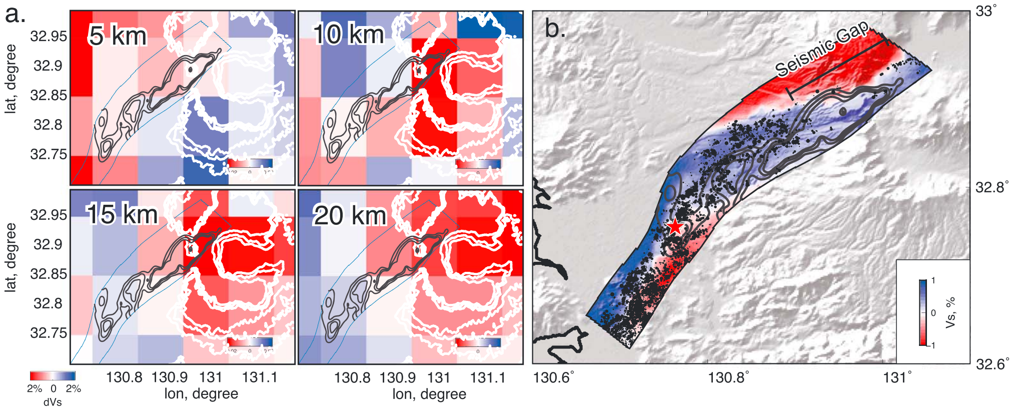

Figure 8. (a) Shear wave velocity (V_s) at each depth are plotted with a blue to red color scale as the background in each panel. In each panel, the coseismic slip pattern is plotted with black contours. The topography contours of the caldera area are plotted in white to indicate the caldera location. (b) Shear wave velocities are interpolated on the fault plane, and the relative V_s perturbation reference to the mean velocity at each depth are plotted with a blue to red color scale. The coseismic slip area is plotted with gray contours. Aftershocks are plotted with black dots. The epicenter is marked with a red filled star. The aftershock gap segment is indicated.

the local shear velocity model (Matsumoto et al., 2015) over the fault plane and overlay the coseismic slip pattern on the mean averaged velocity distribution (Figure 8). The boundary between the high- and low-velocity structures is also identified as the boundary between seismic and aseismic zones. The coseismic ruptures and aftershocks locate within the high-velocity area, while the low-velocity area near the northeastern end of the fault plane appears to be aseismic. In general, the termination of the coseismic rupture correlates with “weak” material properties that are high in temperature and low in resistivity, density, and shear velocity. These material properties may arise from partial melting and ductile deformation behavior. Laboratory experiments demonstrate that wet granite has a low friction coefficient and velocity strengthening property above 350°C (Blanpied et al., 1995). This temperature also appears to be the critical temperature controlling the downdip limit of global seismogenic zones (e.g., Oleskevich et al., 1999). Aseismic creep and ductile deformation are the preferred mechanism to release shear loading for such weak materials, which is also observed in the postseismic period as discussed in the following sections.

We also note that the coseismic rupture initiated in a relatively flat area and terminated under the caldera undergoing a significant ($>$1,000 m) change in topography. The rupture process may be influenced by the topographic stresses. In principle, the crustal stress status can be estimated as the summation of tectonic stress loading, lithostatic stress, topographic stress, and isostatic compensational stresses (Luttrell et al., 2011; Styron & Hetland, 2015). Initial stress status on the fault plane controls the dynamic rupture process, which is also influenced by the stress loading and releasing history during earthquake cycles. Discussion about the complete stress status in the Kumamoto source region is complicated and beyond the scope of this paper. In the following section, we focus on the effect of topographic stresses based on the following considerations: (1) The stress loading and releasing on the fault plane near MTL are mostly in the strike-slip direction, yet topographic stresses are most significantly projected to the fault normal and normal-faulting directions; therefore; stress in these two directions can be estimated without considering tectonic loading. (2) Isostatic compensation occurred beneath the continental crust ($>$30 km depths); thus, the associated stresses have secondary effects to the shallow ruptures ($<$10 km), in comparison with the topographic stresses. (3) Topographic stresses can be estimated analytically with the current available data sets, yet none of other factors can be quantitatively calculated without strong assumptions. Topographic stress is used to estimate the absolute background stress status for the 2008 Wenchuan earthquake (Styron & Hetland, 2015) and 2010 Maule earthquake (Luttrell et al., 2011). It is also found to be controlling the background seismicity in the Himalayan region (Bollinger et al., 2004). We calculate the topographic stress anomalies using Boussinesq approximation (Boussinesq, 1885), by which the topographic weight at each surface point is estimated as a vertical point force loaded on top of a half space. Horizontal stress loading depends on the coupling mechanism between the mountain and the ground surface (Liu & Zoback, 1992), which is generally considered as second-order effects and neglected in this study. Point force amplitude is calculated using mountain

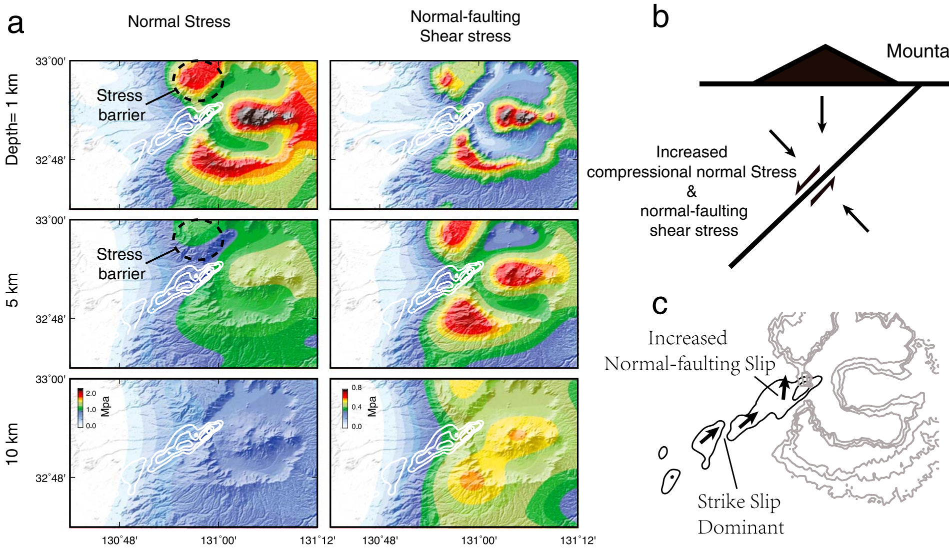

Figure 9. (a) Topographic stress anomalies are calculated for each depth and projected to the fault normal and shear directions to calculate compressional normal stress and normal-faulting shear stress. Relative stresses reference to that at the epicenter are plotted with a white to black color scale for each depth in each row, respectively. Normal stress and normal-faulting shear stress are plotted in the left and right columns, respectively. (b) Cartoon showing the referred focal mechanism under a topographic weight. Compressional stress in the fault normal direction and normal-fault shear stresses are increased by topographic weight. (c) Cartoon showing the slip direction change over the mainshock rupture process. The initial rupture is dominated by strike-slip rupture while the later portion presents increased normal-faulting slips.

weight. Distributed full stress tensors (3 × 3 stress tensors) in response to point force loading are calculated at each depth analytically and convolved with the elevation distribution. Stress tensors are then projected to the fault plane (strike = 220°, dip = 65°) to calculate the fault normal stresses and shear stresses in the normal-faulting direction (Figure 9a), respectively. Stresses at the epicenter are removed from the stress field to estimate relative topographic stresses. We observe substantial amount of normal stress increase (compressional 1–3 MPa) and normal-faulting shear stress increase (0.2–1.0 MPa) under the caldera. These values are at the same order of magnitude of earthquake stress drops (3–10 MPa; Kanamori & Anderson, 1975), which are large enough to influence the coseismic ruptures. High compressional normal stresses increase frictional stresses, thus increasing the failing criteria and acting as a “stress barrier.” Ruptures may be halted or stopped by such stress barriers (Lapusta & Liu, 2009; Styron & Hetland, 2015). The comparison between the coseismic slip model and the topographic stresses suggests that the rupture termination may be related to the topographic “stress barrier,” providing an additional mechanism for the termination of the Kumamoto earthquake.

Topographic weight also increases shear stress in the normal-faulting direction. The Futagawa–Hinagu fault is a strike-slip fault with the tectonic loading in strike-slip sense. This is revealed by the focal mechanism of background seismicity (Matsumoto et al., 2015), major foreshocks, and the initial slip direction (first to third asperities) of the mainshock (Figures 5 and 9). The topography weight adds normal-faulting shearing to the background strike-slip shearing, which appears to increase the normal-faulting slips (fourth asperity) of the mainshock ruptures (Figure 9c). Coseismic displacement is small in comparison with the topographic height; thus, the influence from topographic weight is not released by earthquake cycles, which produce a persistent stress modification over earthquake cycles. The correlation between topographic stresses and the rupture termination indicates that topographic stress is likely an important factor controlling the dynamic rupture process.

3.5. Effect of Material and Stress Barriers

The dynamic rupture of the Kumamoto mainshock appears to be stopped by a rupture barrier. In previous sections, we discussed the possibility of two mechanisms that can produce such a barrier: ductile material properties (a material barrier) or high compressional stresses (a stress barrier; Figure 10). In the following section, we use conceptual fault models to discuss the effect of those barriers on the stress accumulating and

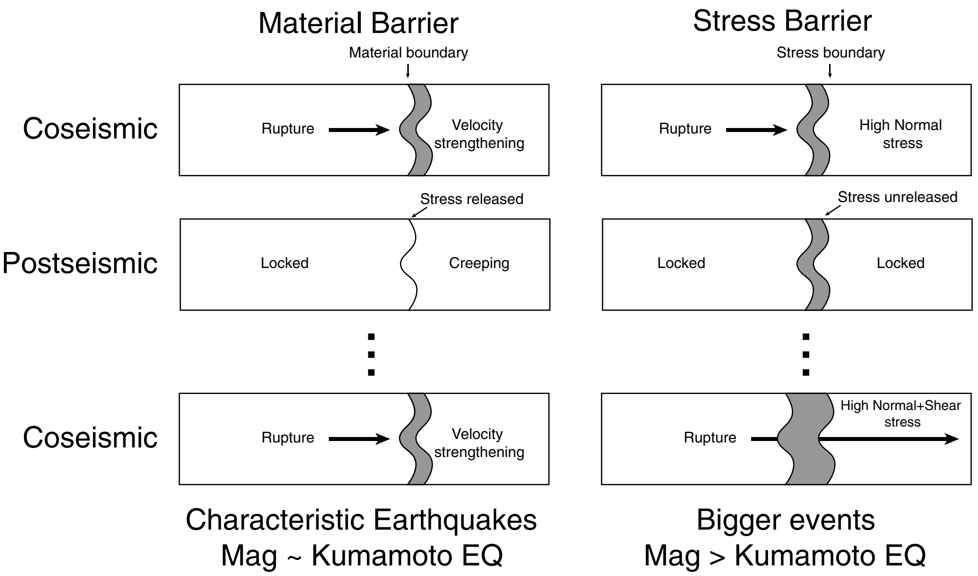

Figure 10. Conceptual end-member models showing the effect of material and stress barriers on the behavior of earthquake cycles. Material and stress barrier behaviors are shown in the left and right columns, respectively. For the material barrier, stress concentration near the rupture tips is released in the postseismic deformation. Each major event in the earthquake cycle is terminated by the material barrier. For the stress barrier, stress concentration near the rupture tips are not released in the postseismic or interseismic period. Such stress concentration accumulates with earthquake cycles and is eventually released by a bigger event.

releasing behavior over earthquake cycles. We consider two plane faults, the right portions of which are covered by either material or stress barriers. As end-member conceptual models, the attributes related to “material” and “stress” barriers are considered as the only nonhomogeneous attributes, and we focus on the discussion about the specific effect of the “barriers.” The “material barrier” is considered as a patch characterized with velocity strengthening property in contrast to the other parts that is characterized with velocity weakening property; the “stress barrier” is considered as a patch with high compressional fault normal stresses on the fault plane, while the whole fault plane is characterized with velocity weakening property. High normal stress introduces high frictional stress, which requires more work to initiate the weakening process, thus producing a high failure criterion. Earthquakes are initiated on the left side and propagated to the right. For the material barrier, shear stresses are released by aseismic creeps during interseismic period (Lapusta & Liu, 2009). During dynamic ruptures, two mechanisms contribute to the rupture termination: limited initial stress and velocity strengthening frictional properties. Stress concentrations are formed near the rupture tip and released through postseismic deformation. Dynamic rupture of the next earthquake cycle is likely to be stopped at the same boundary (Kaneko et al., 2010). In such cases, large events in the earthquake cycle are stopped by the same material barrier and produce identical magnitude, which produces a sequence of characteristic earthquakes (Figure 11a). For the stress barrier model, the barrier is locked in the interseismic period, and the shear stress is not released. A strong enough stress barrier can halt or stop the dynamic rupture process near the patch boundary (Lapusta & Liu, 2009). The stress barrier is fully locked in the postseismic and interseismic periods, and the stress concentration is not released by creeps. Similar phenomena are observed at the updip portion of the 2015 Gorkha earthquake (Gualandi et al., 2016). Shear stress continues to build up through earthquake cycles and approaches the failing criteria. One “regular” event occurred at a “right” time may break through the barrier and rupture with much larger magnitude than previous events. The 2008 M_w = 7.9 Wenchuan earthquake appears to be one such event (Shen et al., 2009). Fault junctions along the Longmenshan fault cause curvatures of the fault plane, and the tectonic loading produces concentrated compressional stress at those junctions. Slip maxima during the Wenchuan earthquake occurred at those junctions, which indicates that Wenchuan earthquake is the “characteristic” event that break through those stress barriers. In this case, bended fault geometry appears to be the key factor introducing stress barriers of the Wenchuan earthquake.

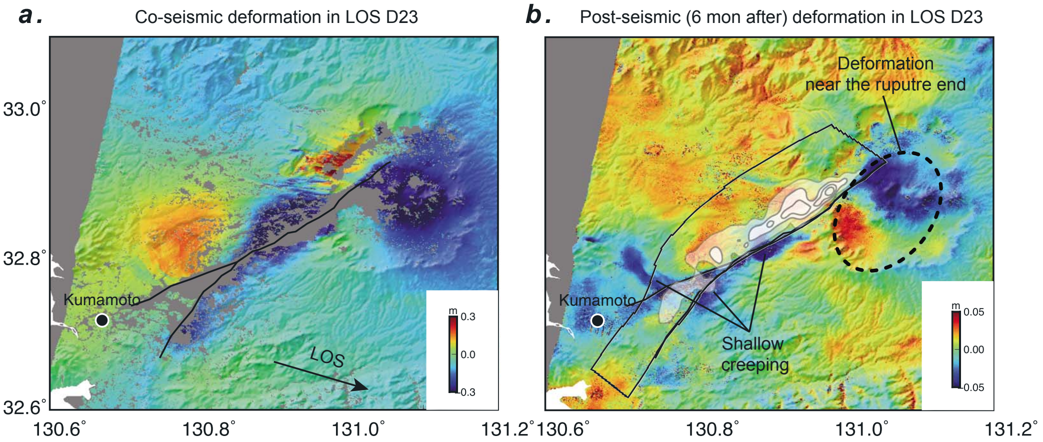

Figure 11. (a) Coseismic displacements recorded by ALOS2 SAR satellite on a descending orbit (path D23). (b) Postseismic ground deformation pattern recorded at the same orbit. Displacements are plotted with different blue to red color scale in both figures. In the postseismic deformation image, ground deformation near the rupture end and related to the shallow slip deficit is marked. Coseismic slip pattern is plotted with shaded contours.

Material and stress barriers may introduce completely different long-term seismic hazards, although the associated coseismic rupture patterns are similar for regular events. Therefore, when a barrier is identified on a fault, it is important to discriminate if it is a material or stress barrier. As demonstrated in Figure 10, material and stress barriers have different frictional behaviors producing different after-slip patterns. Therefore, material and stress barriers can be discriminated based on whether significant after slips occurred near the rupture ends. We processed a SAR interferogram over 6 months after the mainshock showing postseismic ground deformation near the source area (Figure 11). This was also revealed by SAR time series analysis (Moore et al., 2017). The postseismic deformation field presents localized deformation in comparison with the coseismic deformation field (Figure 11). Subsidence or slip happened close to the surface fault traces, which may be due to after slip at shallow depths related to the shallow slip deficit. Significant deformation is observed near the northeastern end of the fault plane inside the caldera, which is likely related to both the after slip on the main fault plane and ductile deformation under the Aso volcano (Moore et al., 2017). Although the SW end of the fault plane presents dense aftershock activities, the observed ground deformation is much smaller than that near the NE end. The observation of significant postseismic deformation demonstrates that a material barrier is likely the mechanism that stops the coseismic rupture. The after slip related to the deformation near the volcano appears to be complementary to the mainshock slip pattern (Moore et al., 2017), which is also consistent with the behavior of a material barrier (Figure 10). Viscoelastic relaxation and poroelastic diffusion need to be considered to model the postseismic ground deformation properly, which should be investigated in further studies. The postseismic deformation observed near the northeastern end of the coseismic rupture demonstrates that stress concentration buildup near the rupture termination is being released by postseismic deformation, which mitigates the concern that a potential large event can occur following the Kumamoto earthquake or in another earthquake cycle.

4. Conclusion

We present a high-resolution kinematic slip model of the mainshock and foreshocks of the Kumamoto earthquake sequence. A unilateral rupture process is resolved for the mainshock, which is composed of sequential rupture of four asperities. The coseismic slip area of the mainshock, foreshocks, and aftershocks form a complementary pattern consistent with Coulomb stress triggering relationship. A gap of aftershocks is resolved to the NE of the end of the coseismic rupture, where the coseismic Coulomb stress is significantly increased. This identified aseismic area is characterized by high temperature and low velocity, gravity, and resistivity, which may be related to the presence of partial melting. Ductile material property may be related to the termination of coseismic rupture. The high topography of the caldera area appears to be related to the increased normal slip component we imaged at the northeastern end of the coseismic rupture.

The effects of both material and stress barriers are discussed in terms of the influence on the stress accumulation and releasing behaviors over earthquake cycle, which emphasize the need to discriminate between these two types of barriers. Evidence from postseismic deformation demonstrates that significant postseismic deformation has happened near the volcano area, which is consistent with the expected postseismic deformation at a material barrier. Therefore, the ductile material property near the caldera area appears to be the dominant mechanism related to the termination of the coseismic rupture.

Acknowledgments
Data analysis made use of GMT, SAC, and Matlab. The strong motion data are recorded by K-net and KiK-net and accessed through NIED. All original GEONET RINEX data are provided to Caltech by the Geospatial Information Authority (GSI) of Japan. Original ALOS-2 radar images are copyright 2016 by the Japanese Aerospace Exploration Agency (JAXA) and were provided under JAXA ALOS RA4 projects P1385, P1372, and P1303 and through the CEOS Disasters Seismic Pilot. This work contains Copernicus data from the Sentinel-1A satellite provided by the European Space Agency (ESA). Part of this research was supported by the NASA Earth Surface and Interior focus area and performed at the Jet Propulsion Laboratory, California Institute of Technology. We thank Mark Simons, Hiroo Kanamori, Jean-Philippe Avouac, Donald Helmberger, Jean-Paul Ampuero, Naofumi Aso, and Adriano Gualandi for their suggestive discussion. This work was supported in part by National Basic Research Program of China grant 2012CB417301 and NSF grant 1447107 awarded to Mark Simons and Jean Paul Ampuero.

References

Abe, Y., Ohkura, T., Shibutani, T., Hirahara, K., & Kato, M. (2010). Crustal structure beneath Aso caldera, Southwest Japan, as derived from receiver function analysis. *Journal of Volcanology and Geothermal Research*, *195*(1), 1–12. https://doi.org/10.1016/j.jvolgeores.2010.05.011

An, C., Yue, H., Sun, J., Meng, L., & Báez, J. C. (2017). The 2015 Mw 8.3 Illapel, Chile, Earthquake: Direction-Reversed Along-Dip Rupture with Localized Water ReverberationThe 2015 Mw 8.3 Illapel, Chile, Earthquake. *Bulletin of the Seismological Society of America*, *107*(5), 2416–2426.

Ando, R., & Okuyama, S. (2010). Deep roots of upper plate faults and earthquake generation illuminated by volcanism. *Geophysical Research Letters*, *37*, L10308. https://doi.org/10.1029/2010GL042956

Asano, K., & Iwata, T. (2016). Source rupture processes of the foreshock and mainshock in the 2016 Kumamoto earthquake sequence estimated from the kinematic waveform inversion of strong motion data. *Earth, Planets and Space*, *68*(1), 147. https://doi.org/10.1186/s40623-016-0519-9

Avouac, J. P., Meng, L. S., Wei, S. J., Wang, T., & Ampuero, J. P. (2015). Lower edge of locked Main Himalayan Thrust unzipped by the 2015 Gorkha earthquake. *Nature Geoscience*, *8*(9), 708–711. https://doi.org/10.1038/Ngeo2518

Ayoub, F., Leprince, S., & Avouac, J.-P. (2009). Co-registration and correlation of aerial photographs for ground deformation measurements. *ISPRS Journal of Photogrammetry and Remote Sensing*, *64*(6), 551–560.

Azzaro, R. (1999). Earthquake surface faulting at Mount Etna volcano (Sicily) and implications for active tectonics. *Journal of Geodynamics*, *28*(2-3), 193–213. https://doi.org/10.1016/S0264-3707(98)00037-4

Beroza, G. C., & Mikumo, T. (1996). Short slip duration in dynamic rupture in the presence of heterogeneous fault properties. *Journal of Geophysical Research*, *101*(B10), 22,449–22,460. https://doi.org/10.1029/96JB02291

Bertiger, W., Desai, S. D., Haines, B., Harvey, N., Moore, A. W., Owen, S., & Weiss, J. P. (2010). Single receiver phase ambiguity resolution with GPS data. *Journal of Geodesy*, *84*(5), 327–337. https://doi.org/10.1007/s00190-010-0371-9

Blanpied, M. L., Lockner, D. A., & Byerlee, J. D. (1995). Frictional slip of granite at hydrothermal conditions. *Journal of Geophysical Research*, *100*(B7), 13,045–13,064. https://doi.org/10.1029/95JB00862

Bollinger, L., Avouac, J., Cattin, R., & Pandey, M. (2004). Stress buildup in the Himalaya. *Journal of Geophysical Research*, *109*, B11405. https://doi.org/10.1029/2003JB002911

Boussinesq, J. (1885). *Application des potentiels à l'étude de l'équilibre et du mouvement des solides élastiques: principalement au calcul des déformations et des pressions que produisent, dans ces solides, des efforts quelconques exercés sur une petite partie de leur surface ou de leur intérieur: mémoire suivi de notes étendues sur divers points de physique, mathematique et d'analyse*. Gauthier-Villars.

Desai, S., Bertiger, W., Haines, B., Harvey, N., Kuang, D., Lane, C., … Weiss, J. (2009). The JPL IGS analysis center: Results from the reanalysis of the global GPS network. *Legacy*, *25*, 30.

Duquesnoy, T., Barrier, E., Kasser, M., Aurelio, M., Gaulon, R., Punongbayan, R., & Rangin, C. (1994). Detection of creep along the Philippine fault: First results of geodetic measurements on Leyte island, central Philippine. *Geophysical Research Letters*, *21*(11), 975–978. https://doi.org/10.1029/94GL00640

Ekström, G., Nettles, M., & Dziewoński, A. (2012). The global CMT project 2004–2010: Centroid-moment tensors for 13,017 earthquakes. *Physics of the Earth and Planetary Interiors*, *200*, 1–9.

Fielding, E. J., Lundgren, P. R., Bürgmann, R., & Funning, G. J. (2009). Shallow fault-zone dilatancy recovery after the 2003 Bam earthquake in Iran. *Nature*, *458*(7234), 64–68. https://doi.org/10.1038/nature07817

Fujiwara, H., Kawai, S., Aoi, S., Morikawa, N., Senna, S., Azuma, H., … Maeda, T. (2009). Technical note of the National Research Institute for Earth Science and Disaster Prevention.

Fujiwara, H., Kawai, S., Aoi, S., Morikawa, N., Senna, S., Azuma, H., … Maeda, T. (2012). Some improvements of seismic hazard assessment based on the 2011 Tohoku earthquake. *Technical note of the National Research Institute for Earth Science and Disaster Prevention*, *379*, 1–349.

Gualandi, A., Avouac, J.-P., Galetzka, J., Genrich, J. F., Blewitt, G., Adhikari, L. B., … Pratt-Sitaula, B. (2016). Pre- and post-seismic deformation related to the 2015, M_w 7. 8 Gorkha earthquake, Nepal. *Tectonophysics*, *714–715*, 90–106.

Hao, J., Ji, C., & Yao, Z. (2017). Slip history of the 2016 M_w 7.0 Kumamoto earthquake: Intraplate rupture in complex tectonic environment. *Geophysical Research Letters*, *44*, 743–750. https://doi.org/10.1002/2016GL071543

Hartzell, S. H., & Heaton, T. H. (1983). Inversion of strong ground motion and teleseismic waveform data for the fault rupture history of the 1979 Imperial Valley, California, earthquake. *Bulletin of the Seismological Society of America*, *73*(6A), 1553–1583.

Hata, M., Takakura, S., Matsushima, N., Hashimoto, T., & Utsugi, M. (2016). Crustal magma pathway beneath Aso caldera inferred from three-dimensional electrical resistivity structure. *Geophysical Research Letters*, *43*, 10,720–10,727. https://doi.org/10.1002/2016GL070315

Himematsu, Y., & Furuya, M. (2016). Fault source model for the 2016 Kumamoto earthquake sequence based on ALOS-2/PALSAR-2 pixel-offset data: Evidence for dynamic slip partitioning (EPSP-D-16-00163). *Earth, Planets and Space*, *68*(1), 169. https://doi.org/10.1186/s40623-016-0545-7

Hsu, Y.-J., Simons, M., Avouac, J.-P., Galetzka, J., Sieh, K., Chlieh, M., … Bock, Y. (2006). Frictional afterslip following the 2005 Nias-Simeulue earthquake, Sumatra. *Science*, *312*(5782), 1921–1926. https://doi.org/10.1126/science.1126960

Kanamori, H., & Anderson, D. L. (1975). Theoretical basis of some empirical relations in seismology. *Bulletin of the Seismological Society of America*, *65*(5), 1073–1095.

Kaneko, Y., & Fialko, Y. (2011). Shallow slip deficit due to large strike-slip earthquakes in dynamic rupture simulations with elasto-plastic off-fault response. *Geophysical Journal International*, *186*(3), 1389–1403. https://doi.org/10.1111/j.1365-246X.2011.05117.x

Kaneko, Y., Avouac, J.-P., & Lapusta, N. (2010). Towards inferring earthquake patterns from geodetic observations of interseismic coupling. *Nature Geoscience*, *3*(5), 363–369. https://doi.org/10.1038/ngeo843

Kato, A., Fukuda, J. I., Nakagawa, S., & Obara, K. (2016). Foreshock migration preceding the 2016 M_w 7.0 Kumamoto earthquake, Japan. *Geophysical Research Letters*, *43*, 8945–8953. https://doi.org/10.1002/2016GL070079

Kubo, H., Suzuki, W., Aoi, S., & Sekiguchi, H. (2016). Source rupture processes of the 2016 Kumamoto, Japan, earthquakes estimated from strong-motion waveforms. *Earth, Planets and Space*, *68*(1), 161. https://doi.org/10.1186/s40623-016-0536-8

Kumahara, Y., Goto, H., Nakata, T., Ishiguro, S., Ishimura, D., Ishiyama, T., … Kaneda, H. (2016). Distribution of surface rupture associated the 2016 Kumamoto earthquake and its significance. Paper presented at Japan Geoscience Union meeting, Chiba, Japan.

Lapusta, N., & Liu, Y. (2009). Three-dimensional boundary integral modeling of spontaneous earthquake sequences and aseismic slip. *Journal of Geophysical Research*, *114*, B09303. https://doi.org/10.1029/2008JB005934

Lapusta, N., Rice, J. R., Ben-Zion, Y., & Zheng, G. (2000). Elastodynamic analysis for slow tectonic loading with spontaneous rupture episodes on faults with rate- and state-dependent friction

Lawson, C. L., & Hanson, R. J. (1995). *Solving least squares problems*, SIAM.

Leprince, S., Barbot, S., Ayoub, F., & Avouac, J.-P. (2007). Automatic and precise orthorectification, coregistration, and subpixel correlation of satellite images, application to ground deformation measurements. *IEEE Transactions on Geoscience and Remote Sensing*, *45*(6), 1529–1558.

Liang, C., & Fielding, E. J. (2016). Interferometric processing of ScanSAR data using Stripmap processor: New insights from coregistration. *IEEE Transactions on Geoscience and Remote Sensing*, *54*(7), 4343–4354. https://doi.org/10.1109/TGRS.2016.2539962

Lin, A., Satsukawa, T., Wang, M., Asl, Z. M., Fueta, R., & Nakajima, F. (2016). Co-seismic rupturing stopped by Aso volcano during the 2016 M_w 7.1 Kumamoto earthquake, Japan. *Science*, *354*(6314), 869–874. https://doi.org/10.1126/science.aah4629

Linde, A. T., & Sacks, I. S. (1998). Triggering of volcanic eruptions. *Nature*, *395*(6705), 888–890. https://doi.org/10.1038/27650

Liu, L., & Zoback, M. D. (1992). The effect of topography on the state of stress in the crust: application to the site of the Cajon Pass Scientific Drilling Project. *Journal of Geophysical Research*, *97*(B4), 5095–5108.

Luttrell, K. M., Tong, X., Sandwell, D. T., Brooks, B. A., & Bevis, M. G. (2011). Estimates of stress drop and crustal tectonic stress from the 27 February 2010 Maule, Chile, earthquake: Implications for fault strength. *Journal of Geophysical Research*, *116*, B11401. https://doi.org/10.1029/2011JB008509

Marone, C. (1998). Laboratory-derived friction laws and their application to seismic faulting. *Annual Review of Earth and Planetary Sciences*, *26*(1), 643–696. https://doi.org/10.1146/annurev.earth.26.1.643

Matsumoto, S., Nakao, S., Ohkura, T., Miyazaki, M., Shimizu, H., Abe, Y., … Yamashita, Y. (2015). Spatial heterogeneities in tectonic stress in Kyushu, Japan and their relation to a major shear zone. *Earth, Planets and Space*, *67*(1), 172. https://doi.org/10.1186/s40623-015-0342-8

Melgar, D., Fan, W., Riquelme, S., Geng, J., Liang, C., Fuentes, M., … Fielding, E. J. (2016). Slip segmentation and slow rupture to the trench during the 2015, M_w 8.3 Illapel, Chile earthquake. *Geophysical Research Letters*, *43*, 961–966. https://doi.org/10.1002/2015GL067369

Miyakawa, A., Sumita, T., Okubo, Y., Okuwaki, R., Otsubo, M., Uesawa, S., & Yagi, Y. (2016). Volcanic magma reservoir imaged as a low-density body beneath Aso volcano that terminated the 2016 Kumamoto earthquake rupture. *Earth, Planets and Space*, *68*(1), 208. https://doi.org/10.1186/s40623-016-0582-2

Moore, J. D., Yu, H., Tang, C.-H., Wang, T., Barbot, S., Peng, D., … Lambert, V. (2017). Imaging the distribution of transient viscosity after the 2016 M_w 7.1 Kumamoto earthquake. *Science*, *356*(6334), 163–167. https://doi.org/10.1126/science.aal3422

Moran, S., Stihler, S., & Power, J. (2002). A tectonic earthquake sequence preceding the April–May 1999 eruption of Shishaldin volcano, Alaska. *Bulletin of Volcanology*, *64*(8), 520–524.

Nishigami, K. y. (1997). Spatial distribution of coda scatterers in the crust around two active volcanoes and one active fault system in central Japan: Inversion analysis of coda envelope. *Physics of the Earth and Planetary Interiors*, *104*(1-3), 75–89. https://doi.org/10.1016/S0031-9201(97)00058-7

Nishimura, S., & Hashimoto, M. (2006). A model with rigid rotations and slip deficits for the GPS-derived velocity field in southwest Japan. *Tectonophysics*, *421*(3-4), 187–207. https://doi.org/10.1016/j.tecto.2006.04.017

Okada, A. (1973). On the quaternary faulting along the median tectonic line. *Median Tectonic Line*, 49–86.

Okubo, Y., Tsu, H., & Ogawa, K. (1989). Estimation of Curie point temperature and geothermal structure of island arcs of Japan. *Tectonophysics*, *159*(3-4), 279–290. https://doi.org/10.1016/0040-1951(89)90134-0

Oleskevich, D., Hyndman, R., & Wang, K. (1999). The updip and downdip limits to great subduction earthquakes: Thermal and structural models of Cascadia, south Alaska, SW Japan, and Chile. *Journal of Geophysical Research*, *104*(B7), 14,965–14,991. https://doi.org/10.1029/1999JB900060

Perfettini, H., & Avouac, J. P. (2004). Post-seismic relaxation driven by brittle creep: A possible mechanism to reconcile geodetic measurements and the decay rate of aftershocks, application to the Chi-Chi earthquake, Taiwan. *Journal of Geophysical Research*, *109*(B2), B02034. https://doi.org/10.1029/2003JB002488

Perfettini, H., & Avouac, J. P. (2007). Modeling afterslip and aftershocks following the 1992 Landers earthquake. *Journal of Geophysical Research*, *112*, B07409. https://doi.org/10.1029/2006JB004399

Rice, J. R. (1993). Spatio-temporal complexity of slip on a fault. *Journal of Geophysical Research*, *98*(B6), 9885–9907. https://doi.org/10.1029/93JB00191

Rice, J. R., Lapusta, N., & Ranjith, K. (2001). Rate and state dependent friction and the stability of sliding between elastically deformable solids. *Journal of the Mechanics and Physics of Solids*, *49*(9), 1865–1898. https://doi.org/10.1016/S0022-5096(01)00042-4

Ross, Z. E., White, M. C., Vernon, F. L., & Ben-Zion, Y. (2016). An improved algorithm for real-time S-wave picking with application to the (augmented) ANZA network in southern California. *Bulletin of the Seismological Society of America*, *106*(5), https://doi.org/10.1785/0120150230

Rosen, P. A., Gurrola, E., Sacco, G. F., & Zebker, H. (2012). The InSAR scientific computing environment. Paper presented at the 9th European Conference on Synthetic Aperture Radar (EUSAR), 2012*, VDE*.

Schmid, R., Steigenberger, P., Gendt, G., Ge, M., & Rothacher, M. (2007). Generation of a consistent absolute phase-center correction model for GPS receiver and satellite antennas. *Journal of Geodesy*, *81*(12), 781–798. https://doi.org/10.1007/s00190-007-0148-y

Shelly, D. R., Hardebeck, J. L., Ellsworth, W. L., & Hill, D. P. (2016). A new strategy for earthquake focal mechanisms using waveform-correlation-derived relative polarities and cluster analysis: Application to the 2014 Long Valley Caldera earthquake swarm. *Journal of Geophysical Research: Solid Earth*, *121*, 8622–8641. https://doi.org/10.1002/2016JB013437

Shen, Z.-K., Sun, J., Zhang, P., Wan, Y., Wang, M., Bürgmann, R., … Wang, Q. (2009). Slip maxima at fault junctions and rupturing of barriers during the 2008 Wenchuan earthquake. *Nature Geoscience*, *2*(10), 718–724. https://doi.org/10.1038/ngeo636

Shi, Q., Wei, S., Lindsey, E., Feng, L., Wang, T., Wang, Y., … Hill, E. (2016). The 2016 Kumamoto earthquake sequence: A series of cross-fault and in-fault triggering events. Abstract S21A-2680 Presented at the 2016 AGU Fall Meeting, San Francisco, CA.

Shirahama, Y., Yoshimi, M., Awata, Y., Maruyama, T., Azuma, T., Miyashita, Y., … Ochi, T. (2016). Characteristics of the surface ruptures associated with the 2016 Kumamoto earthquake sequence, central Kyushu, Japan. *Earth, Planets and Space*, *68*(1), 191.

Stein, R. S., King, G. C., & Lin, J. (1994). Stress triggering of the 1994 $M = 6.7$ Northridge, California, earthquake by its predecessors. *Science-New York Then Washington*, *265*, 1432–1435.

Styron, R. H., & Hetland, E. A. (2015). The weight of the mountains: Constraints on tectonic stress, friction, and fluid pressure in the 2008 Wenchuan earthquake from estimates of topographic loading. *Journal of Geophysical Research: Solid Earth*, *120*, 2697–2716. https://doi.org/10.1002/2014JB011338

Sudo, Y. (1991). An attenuating structure beneath the Aso caldera determined from the propagation of seismic waves. *Bulletin of Volcanology*, *53*(2), 99–111.

Sudo, Y., & Kong, L. (2001). Three-dimensional seismic velocity structure beneath Aso volcano, Kyushu, Japan. *Bulletin of Volcanology*, *63*(5), 326–344. https://doi.org/10.1007/s004450100145

Toda, S., Kaneda, H., Okada, H., Ishimura, D., & Mildon, Z. (2016). Slip-partitioned surface ruptures for the Mw 7.0 2016 Kumamoto, Japan, earthquake. Abstract S52C-04 Presented at the 2016 AGU Fall Meeting, San Francisco, CA.

Trugman, D. T., & Shearer, P. M. (2017). GrowClust: A hierarchical clustering algorithm for relative earthquake relocation, with application to the Spanish Springs and Sheldon, Nevada, earthquake sequences. *Seismological Research Letters*, *88*(2A), 379–391. https://doi.org/10.1785/0220160188

Tsutsui, T., & Sudo, Y. (2004). Seismic reflectors beneath the central cones of Aso volcano, Kyushu, Japan. *Journal of Volcanology and Geothermal Research*, *131*(1-2), 33–58. https://doi.org/10.1016/S0377-0273(03)00315-9

Unglert, K., Savage, M., Fournier, N., Ohkura, T., & Abe, Y. (2011). Shear wave splitting, v_P/v_S, and GPS during a time of enhanced activity at Aso caldera, Kyushu. *Journal of Geophysical Research*, *116*, B11203. https://doi.org/10.1029/2011JB008520

Wallace, L. M., Ellis, S., Miyao, K., Miura, S., Beavan, J., & Goto, J. (2009). Enigmatic, highly active left-lateral shear zone in southwest Japan explained by aseismic ridge collision. *Geology*, *37*(2), 143–146. https://doi.org/10.1130/G25221A.1

Wang, R., Martı´n, F. L., & Roth, F. (2003). Computation of deformation induced by earthquakes in a multi-layered elastic crust—FORTRAN programs EDGRN/EDCMP. *Computers and Geosciences*, *29*(2), 195–207. https://doi.org/10.1016/S0098-3004(02)00111-5

Wei, M., Sandwell, D., Fialko, Y., & Bilham, R. (2011). Slip on faults in the Imperial Valley triggered by the 4 April 2010 M_w 7.2 El Mayor-Cucapah earthquake revealed by InSAR. *Geophysical Research Letters*, *38*(1), L01308. https://doi.org/10.1029/2010GL045235

Wei, S., Fielding, E., Leprince, S., Sladen, A., Avouac, J.-P., Helmberger, D., … Hudnut, K. (2011). Superficial simplicity of the 2010 El Mayor-Cucapah earthquake of Baja California in Mexico. *Nature Geoscience*, *4*(9), 615–618. https://doi.org/10.1038/ngeo1213

Wibberley, C. A., & Shimamoto, T. (2003). Internal structure and permeability of major strike-slip fault zones: The median tectonic line in Mie Prefecture, Southwest Japan. *Journal of Structural Geology*, *25*(1), 59–78. https://doi.org/10.1016/S0191-8141(02)00014-7

Yagi, Y., Okuwaki, R., Enescu, B., Kasahara, A., Miyakawa, A., & Otsubo, M. (2016). Rupture process of the 2016 Kumamoto earthquake in relation to the thermal structure around Aso volcano. *Earth, Planets and Space*, *68*(1), 1–6.

Yue, H. (2014). Toward resolving stable high-resolution kinematic rupture models of large earthquakes by joint inversion of seismic, geodetic and tsunami observations (PhD thesis).

Yue, H., & Lay, T. (2013). Source rupture models for the M_w 9.0 2011 Tohoku earthquake from joint inversions of high-rate geodetic and seismic data. *Bullitin of Society of Seismology America*, *103*(2B), 1242–1255. https://doi.org/10.1785/0120120119

Yue, H., Lay, T., Freymueller, J. T., Ding, K., Rivera, L., Ruppert, N. A., & Koper, K. D. (2013). Supershear rupture of the 5 January 2013 Craig, Alaska (M_w 7.5) earthquake. *Journal of Geophysical Research: Solid Earth*, *118*, 5903–5919. https://doi.org/10.1002/2013JB010594

Yue, H., Lay, T., Schwartz, S. Y., Rivera, L., Protti, M., Dixon, T. H., … Newman, A. V. (2013). The 5 September 2012 Nicoya, Costa Rica M_w 7.6 earthquake rupture process from joint inversion of high-rate GPS, strong-motion, and teleseismic *P* wave data and its relationship to adjacent plate boundary interface properties. *Journal of Geophysical Research: Solid Earth*, *118*, 5453–5466. https://doi.org/10.1002/jgrb.50379

Yue, H., Lay, T., Rivera, L., An, C., Vigny, C., Tong, X., & Báez Soto, J. C. (2014). Localized fault slip to the trench in the 2010 Maule, Chile $M_w = 8.8$ earthquake from joint inversion of high-rate GPS, teleseismic body waves, InSAR, campaign GPS, and tsunami observations. *Journal of Geophysical Research: Solid Earth*, *119*, 7786–7804. https://doi.org/10.1002/2014JB011340

Yue, H., Simons, M., Duputel, Z., Jiang, J., Fielding, E., Liang, C., … Ampuero, J. P. (2017). Depth varying rupture properties during the 2015 Mw 7.8 Gorkha (Nepal) earthquake. *Tectonophysics*, *714*, 44–54.

Zhu, L., & Rivera, L. A. (2002). A note on the dynamic and static displacements from a point source in multilayered media. *Geophysical Journal International*, *148*(3), 619–627. https://doi.org/10.1046/j.1365-246X.2002.01610.x

Zumberge, J., Heflin, M., Jefferson, D., Watkins, M., & Webb, F. H. (1997). Precise point positioning for the efficient and robust analysis of GPS data from large networks. *Journal of Geophysical Research*, *102*(B3), 5005–5017. https://doi.org/10.1029/96JB03860